

**The Influence of Asteroid Surface Features on the YORP
Effect and Dynamical Evolution**

by

Dahlia A. Baker

B.A., Coe College, 2018

M.S., University of Colorado Boulder, 2021

A thesis submitted to the
Faculty of the Graduate School of the
University of Colorado in partial fulfillment
of the requirements for the degree of
Doctor of Philosophy

Ann and H.J. Smead Department of Aerospace Engineering Sciences

2024

Committee Members:

Jay W. McMahon, Chair

Dr. Daniel J. Scheeres

Dr. Paul Sanchez

Dr. Paul Hayne

Dr. William Bottke

Baker, Dahlia A. (Ph.D., Aerospace Engineering Sciences)

The Influence of Asteroid Surface Features on the YORP Effect and Dynamical Evolution

Thesis directed by Dr. Jay W. McMahon

Often the abstract will be long enough to require more than one page, in which case the macro “\OnePageChapter” should *not* be used.

But this one isn't, so it should.

Dedication

I dedicate this manuscript to my family. Thank you for your endless support.

Acknowledgements

I'd like to acknowledge my tireless advisor, Jay McMahon, for accepting me to the ORCCA Lab six years ago and letting me do whatever I wanted with my research while supporting me at every step along the way. I have many exciting opportunities ahead of me thanks to you. I thank my colleagues in the ORCCA Lab and CCAR whose advice, collaboration, and kindness made this all possible. Lyss, you deserve the most recognition for your compassion and brilliance and without your friendship, I would not have made it through. I will also honorably mention my professors from the Coe College physics department, who pushed me to continue with my education and became my family in Iowa. Thank you Ugur, Mario, Doc, and Firdevs for your help and friendship. Your commitment to student success and excellence in research is why I got to chase my dreams. Thank you to my partner, Nicholas, for your patience and support as I approach graduation and hesitate to ask for your help with the math. I know that you'd be very helpful but I refuse to add my boyfriend as a co-author. I can't wait to support you through your own journey to your Ph.D. Lastly, I am grateful to my committee members for their guidance and expertise which shapes this work. I hope to continue working on exploring asteroids and staying in this field with you.

Contents

Chapter

1	Introduction and Motivation	1
1.1	Asteroid Surfaces	1
1.1.1	Shape Modeling	2
1.1.2	Dynamics and the YORP Effect	4
1.1.3	Thesis Statement	6
1.1.4	Thesis Overview	6
2	Optical-Based Shape Modeling	7
2.1	Introduction	7
2.2	Methods	7
2.2.1	Assumptions	7
2.2.2	Simulated Image Procedure	8
2.2.3	Mission Data	8
2.2.4	Image Processing - Finding the Silhouette	9
2.2.5	Terminator and Limb Discrimination	13
2.2.6	Ray Generation and Trimming	13
2.2.7	Outlier Rejection	18
2.2.8	Surface Reconstruction	18
2.3	Shape Results	19

2.3.1	Simulated Data	19
2.3.2	Mission Data	22
2.4	Matching Localization	24
2.4.1	Method	24
2.4.2	Results	25
2.5	Analysis	26
2.5.1	Error Evaluation	26
2.6	Discussion	27
2.7	Conclusion and Further Work	27
3	Boulder-Induced YORP Altering Spin Acceleration	29
3.1	Torque Calculation	29
3.2	Boulder Factors	29
4	Pole Stability and Obliquity Evolution under YORP Torques	30
5	Estimates of YORP for Ground-Based Observing	31
6	Future Work	32
 Appendix		
A	Weird Exam Answers	33
B	Ode to Spot	35

Tables

Table

Figures

Figure

2.1	Example Images	9
2.3	25 Examples of Canny Parameters and Impact on Edge Detection	11
2.4	Four Edge Results Overlaid in Image Space	11
2.5	Limb and Terminator in Bennu Mission Image	13
2.6	Geometry of Two Intersecting Planes	14
2.7	Geometric Depiction of Patch Crossing Calculations	16
2.8	Intersection Ray from Two Patches - Ten Sampled Points and Associated Ray Normals	17
2.9	Ball-Pivoting Surface Reconstruction Results of Itokawa and Bennu Point Clouds . .	19
2.10	Pre- and Post-Processed Point Cloud of Itokawa Limb-Trimmed Shape	20
2.11	Limb-based Itokawa shape compared to SPC, with surface error in units of kilometers	21
2.12	Pre- and Post-Processed Point Cloud of Bennu Limb-Trimmed Shape	21
2.13	Limb-based Bennu shape compared to SPC, with surface error in units of kilometers	22
2.14	Bennu Shape Model from Real Images, compared to SPC, surface error in kilometers	23
2.15	Test image and Library Image, Expected Match Pair	26
2.16	Test image and Library image, Actual Match Pair	27
2.17	2D Correlation scores between all library images and all test images, based on longitude	28

Chapter 1

Introduction and Motivation

1.1 Asteroid Surfaces

Studying asteroids is important to understanding the origin of our own planet. They are remnants of the protoplanetary disk, and provide insights as to the composition of the original materials that eventually formed rocky planets as well as gaseous ones. In this work, I will be focusing on the smallest members of the asteroid population and the unique dynamics at play in their evolution. Small asteroids are often made up of many separate particles and boulders which is why they are referred to as "rubble piles" [?]. Often originating from a previous impact event of a parent body, the many pieces come together over time and bond by weak gravity and electrostatic cohesion [?]. These bodies are resilient and active, frequently resurfacing, losing particles, and experiencing further bombardment. By our recent visits to asteroid targets in the sub-1 km size regime, we have seen high-resolution examples of these bodies and been able to characterize the boulders and regolith on their surfaces. These missions produced shape models that enabled both science and navigation. The OSIRIS-REx mission successfully orbited around the 524 m diameter asteroid Bennu for years, measuring the gravitational properties and taking images to constrain the shape [?]. We observed the extremely dark and unexpectedly rocky surface of Bennu and even witnessed particle escape [?]. The sample taken from Bennu has already returned to Earth to undergo testing and characterization which will tell us more about the materials we should expect to find on B-type asteroids like Bennu in the future [?]. Another recent mission that demonstrated the capabilities of asteroid rendezvous and high-resolution shape modeling was Hayabusa2, launched

by JAXA to arrive at Itokawa in 2018 [?]. This mission characterized the irregularly shaped body Itokawa and also furthered asteroid science in unexpected ways.

1.1.1 Shape Modeling

The accurate capture of the surface and bulk shape is an important data product for science and navigation. It enables the precise mapping of the gravity field, and better target characterization for relative navigation solutions (expand this) (cite it). One method for creating a shape model is by the combination of optical images which capture various poses and features of the target body.

When spacecraft are deployed to study small bodies in our solar system, they lose the consistent ability to access classical systems for communication such as the Deep Space Network which relays messages from the ground-based operators. However, as the sensitivity of the actions executed by these spacecraft increases, such as during the Touch-And-Go maneuver that OSIRIS-REx achieved when sampling the surface of Bennu [?], autonomy becomes critical. With radio communications, there is a delay of minutes between sending commands and their execution time which can mean the difference between a landing and a large miss when targeting small bodies for rendezvous or even flybys. This necessary level of autonomy can be achieved by allowing for the onboard processing capabilities that enable navigation and mission-related decision making. Optical information is the primary focus of this study for its advanced development in navigating spacecraft [?], despite its challenges in the space environment [?], where careful planning is required to handle the varying lighting conditions. This work focuses on the construction of the shape model data product during the approach trajectory phase when the body has many pixels of resolution and the silhouette is discernible. This moves away from feature-focused shape modeling approaches such as SPC [?], stereophotogrammetry (shape from motion)[?], and many other algorithms which identify shadows, craters, rocks and boulders, and even ridges in order to inform the shape. These alternate methods use specific feature detector algorithms to identify surface variations mathematically [?]. It is simpler to take advantage of the contrast of a high-albedo body versus a background of space

in order to extract a silhouette which can be identified as the limb and terminator of the observable surface. The capabilities accessed via this data type have been shown in previous limb-focused localization approaches by Christian [?].

Silhouette-based methods of shape modeling are used extensively for the reconstruction of singular objects in the computer vision community[?][?][?]. As the small-body community encounters a similar problem, there is a push to investigate limb information as a solution to onboard processing limitations [?][?]. A shape such as an asteroid or a binary system is a good candidate and many variations of these natural shapes have been investigated by previous studies. Alongside simulated tool development, these practices have been applied in-house for mission data solutions. The OSIRIS-REx mission developed and applied a limb-based tool (LIMBER) to resolve a pre-SPC model with accuracy of 3-4m when image frequency was 10° and the spacecraft was located in a hovering position within 200km from the target [?]. Their approach followed very similar procedure as the work presented here, but was not able to apply information from the terminator. Other teams have focused on a similarly simulated method based on finding the silhouette and carving the 3D shape from a preset voxel cube [?]. The aim of each of these efforts, including the one presented in this paper, is to show that the silhouette information is both robust and computationally efficient as a candidate for onboard processing. However, previous work has highlighted the requirements of the image processing stage when sourcing limb information from optical data [?]. The shape model built using approach observations in the optical range can reach a precision level high enough for navigation purposes with few assumptions at the current stage of development. The future goal is to evolve a dynamic shape model stored onboard, which can be used to inform future navigation decisions; this would improve the overall mapping performance, heightening the autonomy of the mission [?]. In this work, the models presented are generated from simulated data sources and compared to the most resolute shape models available for the bodies in question. The method is tested on both a convex and irregular body in order to show how our overlaid silhouette trimming procedure responds to self-shadowing, the presence of concavity, as well as phase angle projections of the terminator introduced by the orientation of the sun and camera. This algorithm

will be developed as necessary to enable onboard shape model generation, but this paper serves to present and defend the method which uses a process of refinement based on extending the shape along the silhouette cutout in space, and narrowing down the three-dimensional hull through multiple viewing angles. As the small body community looks to grant more SIMPLEX-level missions to asteroids, it is necessary to develop the autonomous onboard navigation capabilities that make those missions possible.

1.1.2 Dynamics and the YORP Effect

Small bodies in our solar system and particularly in the near-earth environment are of interest to scientists for their resources, their connection to the proto-planetary origins of our Earth, and the possible threat of impact with our planet. Many factors make this population difficult to characterize, such as their limited size, low albedo surfaces, and the difficulty of predicting precise orbits due to low frequency of observation and unmodeled forces. Collective survey efforts have yielded a possible 30% of the $\geq 100\text{m}$ population found while the rest remain undiscovered. Observation efforts are increased each year in order to increase the database of known bodies and also our confidence in the dynamics of dangerous suspects that could intersect with our own planet's orbit [?][?]. These efforts reveal new targets for space missions that aim to flyby or rendezvous with small bodies to learn more about their surfaces and possibly conduct sample return for deeper Earth-based compositional analysis. In any case, the entire size range of small bodies is of high interest to the scientific and planetary defense communities. This work focuses on the smallest members of the asteroid population, bodies under 1km in diameter, and the particular thermal interactions changing their orbit in ways that have only recently been observed.

The Yarkovsky-O'Keefe-Radzievskii-Paddack (YORP) effect is an example of a force that becomes dominant for asteroids with a diameter below one kilometer. This recoil force acts to change the spin rate and pole orientation via asymmetries in the shape of a body. The surface imparts additional torque during the process of absorbing and re-radiating thermal energy over the course of it's rotational day and year. The longitudinal asymmetries of the body contribute to the

change in the spin rate, either spinning the body up or down depending on the bias of the features. Spin-pole obliquity change occurs due to global deviations in symmetry, imparting a tilt on the spin axis which could eventually lead to tumbling. Note that the YORP effect is acting purely on the local attitude of the body via interactions with the surface and its irregularities, while the Yarkovsky effect acts on all bodies to cause a change in the semi-major axis of the orbit [?]. We have thus far observed 12 bodies in our solar system that exhibit dynamical changes due to YORP [?]. This is due to the increase in efforts to observe and model the YORP effect. It is shown that YORP is extremely sensitive to small-scale topography such as boulders and craters on the surface, or even a smaller approximation of surface roughness through regolith modeling [?][?][?]. It is of significant interest to characterize YORP accounting for common features of small bodies in the YORP-dominant size regime, such as boulders, craters, and regolith [?]. We choose to investigate the populations and properties of boulders.

Boulders have geological significance because they hold information about local surface processes and natural movement of materials [?]. For the case of small bodies, we assume boulder motion is due to local landslides, regolith redistribution from tidal forces or planetary encounters, and surface sublimation causing fracturing [?] [?]. The parameters of size, shape, texture, and comparative composition are all indicators of the time history of geological evolution for a small body. Boulders have been found on all rubble-pile asteroids and they contribute unique properties thermally, geologically, and dynamically [?]. As fractured protrusions, they absorb and radiate heat tangent to the surface [?]. Their continuous motion and degeneration contributes majorly to the changing shape of small bodies [?] [?][?][?]. Lastly, they are a vehicle of energy dissipation via infilling, escape, and aggregation [?]. Due to the small sample size of observed asteroid surfaces, there is no deterministic way to analyze the boulder distribution on all possible asteroid shapes. The surfaces that are available for analysis come from recent mapping and sample acquisition missions such as OSIRIS-REx which successfully mapped Bennu to a mean accuracy of 30 cm [?]. Despite this, the possible shapes of small bodies in our solar system are highly variable and extremely difficult to constrain from ground-based observations. The approach taken in this work is to develop

statistical approximations for the size and frequency of boulders on an asteroid surface from the currently available image datasets [?][?][?]. This approximation serves to constrain the possible variability in YORP due to boulders for bodies in these size regimes. Rather than using a purely stochastic approach, the uncertainty is informed by Monte Carlo simulation of a known shape decorated with boulder populations following the distributions modeled after real surfaces. We approach the question of YORP variability from a new direction, using observational data to calculate possible bounds on YORP torque due to the additional presence of boulders. We will characterize the magnitude of YORP spin torque due to a singular boulder in different conditions.

1.1.3 Thesis Statement

1.1.4 Thesis Overview

Chapter 2

Optical-Based Shape Modeling

2.1 Introduction

In this work, the models presented are generated from both simulated and actual mission data sources and compared to the most resolute shape models available for the bodies in question. The method is tested on both a convex and irregular body in order to show how our overlaid silhouette trimming procedure responds to self-shadowing, the presence of concavity, as well as phase angles projections introduced by the orientation of the sun and camera. This work will be developed as necessary to enable onboard shape model generation, but this paper serves to present and defend the method which uses a process of refinement based on extending the shape along the silhouette cutout in space, and narrowing down the three-dimensional hull through multiple view angles. As the small body community looks to grant more SIMPLEX level missions to asteroids, such as the Janus mission which will rendezvous with a binary system, it is necessary to develop the autonomous onboard navigation capabilities that make those missions possible.

2.2 Methods

2.2.1 Assumptions

In its current formulation, this shape modeling method processes a batch of optical and infrared images taken at a reasonable distance away from a target body. The body does not need to be centered in the frame of the image, nor does it need to be fully lit. The assumptions made

in the work to follow include full knowledge of the body frame, beginning with the orientation of the spin pole and further defined by convention. The orientation and location of the camera is known along with its frame, as well as the sun location in the body frame. In actual missions, there is a reasonable track of the spacecraft orientation and location in the inertial (sun-centered) frame, and a state estimate is formed for the body during approach and during ground-based observation campaigns. In this work, perfect certainty of the body location, spacecraft location, and the camera-pointing vector can be assumed.

2.2.2 Simulated Image Procedure

Simulated images were necessary to test the robustness of our modeling method. The process of generating these images was performed via Blender software blender with the goal of recreating conditions of the OSIRIS-REx approach phase to the asteroid Bennu. The shape model was of 6m resolution, sourced from the approach data results given by the OSIRIS-REx missionLauretta2019. Lighting conditions, such as the sun location, were manipulated to match the testing criteria but the inherent qualities were kept constant: a light strength of 5 MW, 0% specularity, and a radius of 1m were suitable to illuminate the target for the purpose of recreating mission-similar conditions. Both a regular and irregular body were tested. The camera dimensions were kept in accordance with the PolyCam on the OSIRIS-REx missionRizk2017.

2.2.3 Mission Data

The data obtained to further test the modeling software was sourced from the OSIRIS-REx and Hayabusa mission SPICE archives. Necessary data regarding the camera dimensions, frame-to-frame transformations, the state of the camera, body, and sun were accessed as well as the images themselves which came from the PDS archives but their timestamps allowed for coordination of state and image. Shown below is an example of similarity between the simulated image sets and actual mission data, which proves that moving forward with both can provide comparable results when focusing on the silhouette information.

2.2.4 Image Processing - Finding the Silhouette

The procedure of shape generation using optical data begins with processing the images and finding the desired information - the silhouette of the body. The data shows results where the camera is within 100km, 151km, and 8km of the target body for the simulated test cases, the OSIRIS-REx data, and the Hayabusa images respectively. Examples of the input are shown in Fig. The simulated images and the mission data differ most in their surface detail, where rocks and boulders can be seen readily on mission images but are majorly missing from the surface representations of the shape models processed by Blender. For the purposes of silhouette-based shape modeling, this detail is acceptable and there are many steps implemented to ensure that all data sets are treated equally. This algorithm begins with a pre-processing thresholding procedure. An image is translated from RGB values into grayscale between $[0,255]$ in intensity. These values are then flattened with the lowest intensity pixels (< 2) removed and all other intensities amplified by a factor of 1000. This produces a flat background of space with a bright masked featureless image of the body.

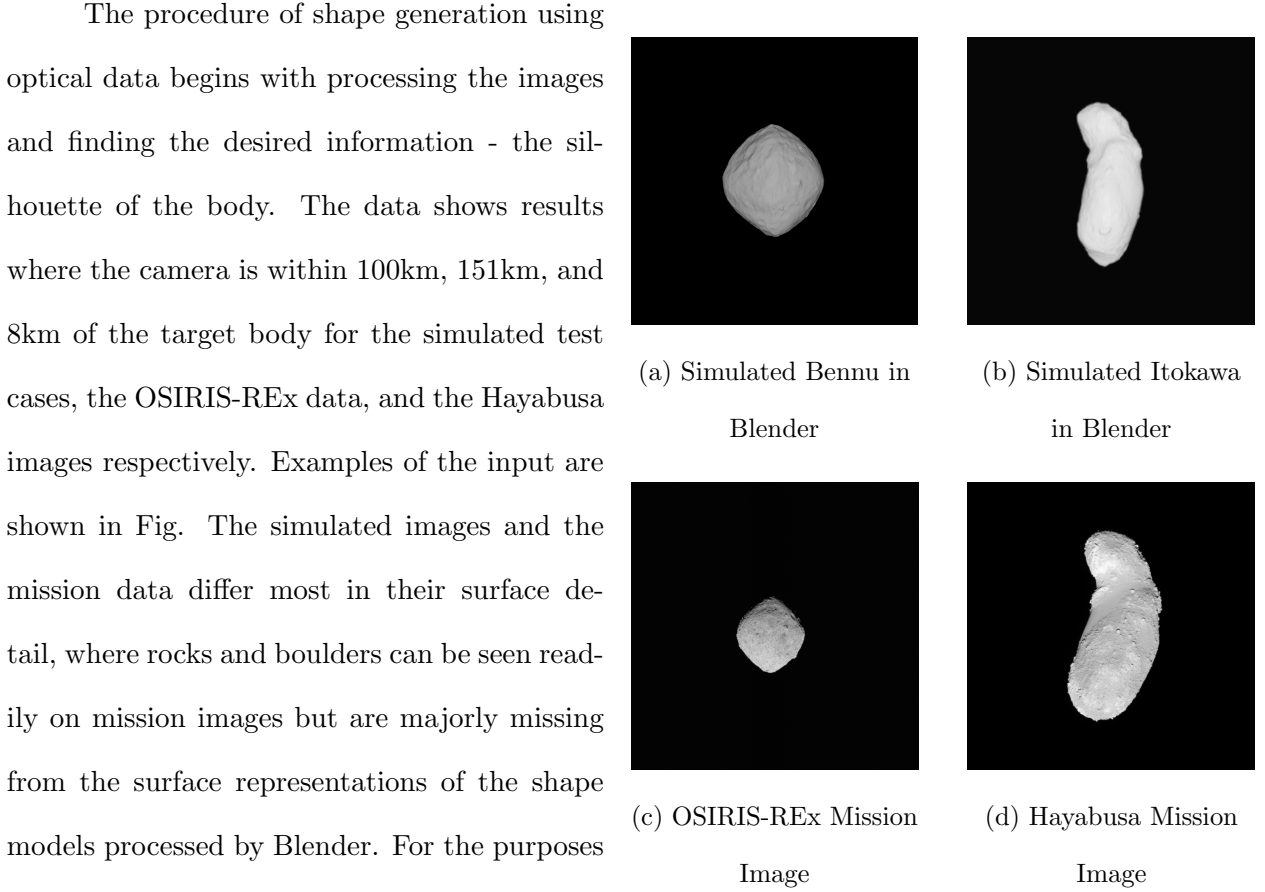
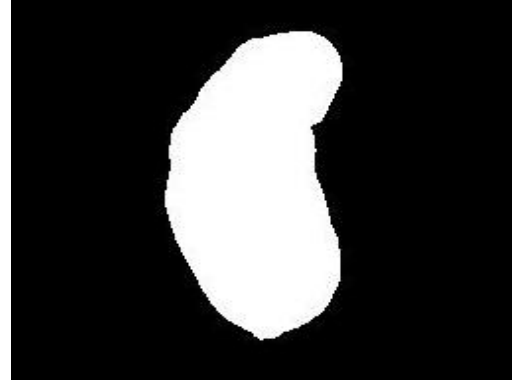


Figure 2.1: Example Images

With a preprocessed, thresholded image, the next step is to apply an edge detection function in



(a) Unprocessed Itokawa Image



(b) Processed Itokawa Image

order to differentiate the silhouette from the background of space. The function used here is the Canny operator, which can be tuned for sensitivities that correspond to the level of detail desired-Canny1986. The Canny algorithm applied via Matlab function involves several steps as follows. The first step is to apply another Gaussian filter to smooth the image and thus reduce noise for calculating the edge locations. The equation for the Gaussian kernel applied to the image is below, for an image of size $(2k+1) \times (2k+1)$:

$$H_{ij} = \frac{1}{2\pi\sigma^2} \exp\left(-\frac{(i - (k+1))^2 + (j - (k+1))^2}{2\sigma^2}\right); 1 \leq i, j \leq (2k+1) \quad (2.1)$$

After the Gaussian noise reduction kernel has been applied, the function needs to find the intensity gradients in the image in order to identify locations of possible edges. The Canny algorithm uses four filters to find four different directions of gradients: vertical, horizontal, and two different diagonal directions. The edge gradient and associated direction is given by the equation which considers both the gradient in the x dimension and the y dimension.

$$G = \sqrt{G_x^2 + G_y^2} \quad (2.2)$$

$$\Theta = \tan^{-1} \frac{G_y}{G_x} \quad (2.3)$$

After the gradient is calculated over the image, the desired thresholding factor is applied to eliminate edges of very low or high intensity. In this approach, it is typical to eliminate a large proportion of low intensity edges which, in the particular data sets applied, corresponds to ridges and boulder

shadows. At the end of the thresholding process, the algorithm can be confident to a significant degree that it has identified the edge of the objects captured in the given image.

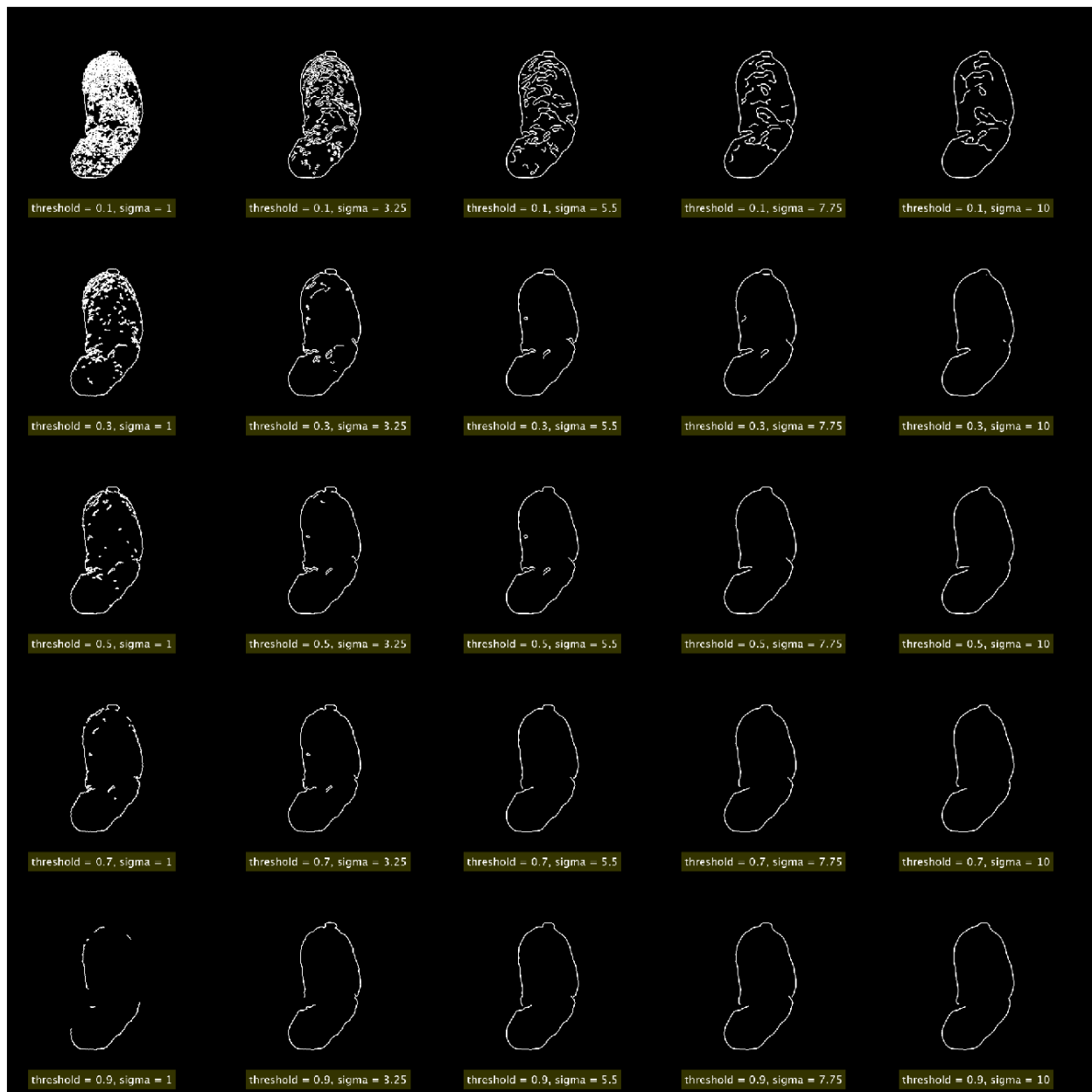


Figure 2.3: 25 Examples of Canny Parameters and Impact on Edge Detection



In order to capture the edge, the Canny operator was tested for effectiveness over many threshold and standard deviations. Examples of these results are given in

Fig. which present the extremes that the function is capable of capturing from the typical asteroid image. The selected values for edge processing were $T=0.5$ and $\sigma = 5$. Combined with the previous thresholding steps that output a flat mask, this operator has no issue identifying an appropriate edge for silhouette finding. After the edge is identified, the points are sorted in unit circle order, beginning at the traditional $+x$ axis and moving counter-clockwise in the (u,v) plane. Each image is subsampled to contain an evenly spaced set of points from the full edge result. This is one way in which the data density is reduced for the purpose of faster processing. The original Canny edge output represents each pixel identified as an edge, which can be thousands of data points.

Taking the four best results from the Canny investigation above, they are overlaid in Fig. to show that differing parameters still provide similar results. The difference between each output is only measured by a few pixels, therefore it can be assumed that the ultimate shape results will not be majorly affected by changing the Canny parameters, as long as the parameters implemented have met the original requirement of identifying only the silhouette and excluding internal features.

After identifying the silhouette in the image frame and thus in the 3-D camera frame with the addition of the range dimension, the points must be translated into the 3-D body frame which is predefined and known prior to processing. This is an assumption made based on the expected capability to obtain lightcurve information both on the ground and early in the flight plan which will inform about the spin pole and allow for a definition of the body frame to be made. However, for the purposes of this work, the body frame is accessed via SPICE and from scientific convention Fujiwara2006Scheeres2006. This transformation allows each image to be considered in the body frame against one another, which is what enables the ray trimming process. The points are extended

towards and away from the camera direction with the center of the ray corresponding to the originally identified edge point.

2.2.5 Terminator and Limb Discrimination

One major known quantity in any space mission is the direction of the sun vector. This is increasingly important for a small body in which the whole shape can be observed along with the terminator, which is dependent on the relationship between the body, the camera, and the sun positions. In this work, it is assumed that there is perfect knowledge of the sun location and thus the unit vector corresponding to the sun direction in the body and image frames. This state allows for a calculation of the phase angle which becomes crucial when differentiating a limb versus a terminator in an image of a body that is only partially lit. The knowledge of the sun unit vector in the camera frame allows for simple vector products to separate the edge points which are facing the sun and the points which are on the opposing side.

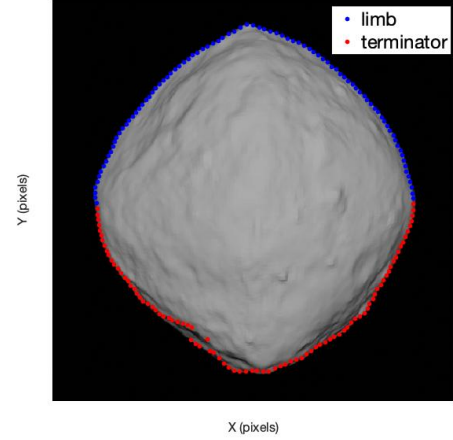


Figure 2.5: Limb and Terminator in Bennu Mission Image

2.2.6 Ray Generation and Trimming

The silhouettes have been identified and placed in their assumed positions in the bodycentric frame of the target, and now the next step is to extend these points into rays which will concentrically constrain the surface McMahon2018. The reason why the rays are necessary is that the points themselves may be misaligned, contain outliers, or possibly not hold enough information to solve for a reasonable resolution of the surface. Extending our points into rays which will be trimmed based on intersections and subsampled allows for more detail without requiring more information.

The rays are described using a line equation to characterize them in 3D body frame space. The equation of the line segments is as follows for i number of rays l in each view.

$$l_i = l_{i,0} + \eta L \hat{r} \quad (2.4)$$

In the above equation, $l_{i,0}$ is the initial point of the ray, η is the scale factor from 0 to 1 describing how far along the rays length it's been trimmed (between 0 and 100 percent), L is the length of the pretrimmed ray, and \hat{r} is a generic unit view direction. For this investigation, the original ray length L is set to 2km, centered at the identified edge point and extended towards and away from the camera for limb points, with terminator points at a slight rotation proportional to the phase angle. The η factor is calculated after finding all intersections between each limb plane and trimming each ray down to it's likely surface section, and this procedure will be described in later sections.

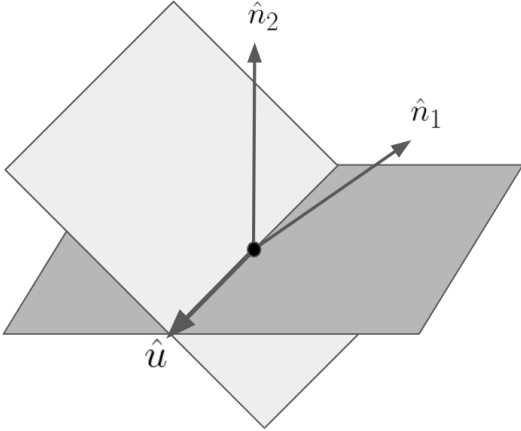


Figure 2.6: Geometry of Two Intersecting Planes

With a sample of N_p edge points, there can be N_p number of planar quadrilaterals formed by connecting each adjacent edge point as seen in Fig. , and calculating its surface normal direction with the following equation:

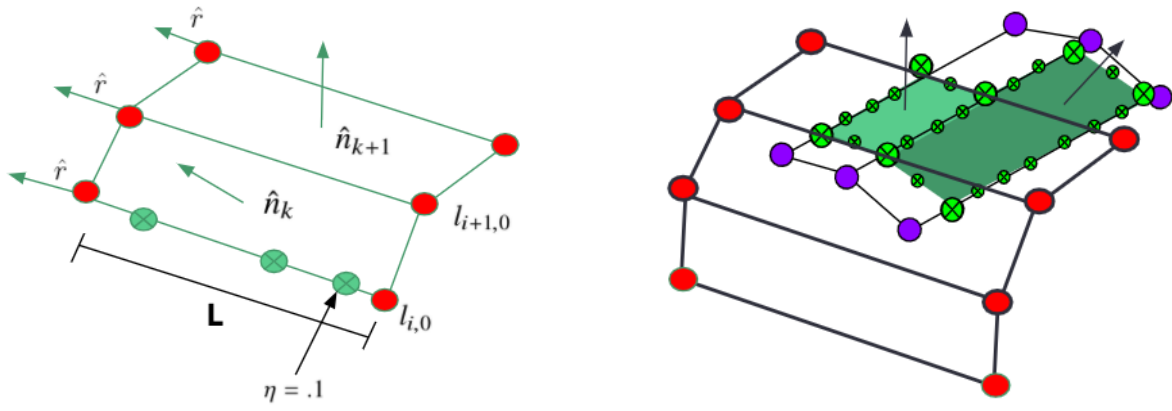
$$\hat{n}_k = \frac{\hat{r} \times (l_{i+1,0} - l_{i,0})}{|\hat{r} \times (l_{i+1,0} - l_{i,0})|} \quad (2.5)$$

The planar quadrilaterals will be referred to as patches in the following discussion. These patches have an associated normal vector, and two rays which describe the lines in the \hat{r} direction. Processing this information in a batch method, all of the rays are iterated through to find where each plane intersects with another plane from the found silhouettes. The locations of the intersection, along with the percentage along the ray that the location is identified, are saved and then evaluated to find where the rays need to be

trimmed away. The line of intersection between two planes in 3D space exists if the cross product of the two normal vectors associated with each plane is nonzero. If $n_1 \times n_2 = 0$, then the two planes in question are parallel and will be ignored. In the implementation presented here, the threshold for a nonzero parallel evaluation is that the magnitude of the cross product of the normal vectors is above 1×10^{-10} . The line of intersection itself also lies along the cross product of the two normal vectors. If an intersection can be found, the η value corresponding how much of the line should be kept is saved, and the rest of the line is trimmed and the equation of this specific line is updated to go between η length and the other remaining end for the next iteration. Now the direction vector of the intersection line can be found using the normal vectors of the two planes, as shown in Eq.3. The variable m gives the direction of slope, and a point on the line is found numerically, which corresponds to b , and from there a whole line equation is given in $y = mx + b$ form.

$$m = \frac{\hat{n}_1 \times \hat{n}_2}{|\hat{n}_1 \times \hat{n}_2|} \quad (2.6)$$

The results from the line intersection calculations are many line equations describing the unit vector corresponding to the direction of the intersection line, the end points of the original rays, and the points corresponding to the physical end of the intersection line for these finite patches. The next step is to evaluate which parts of the ray must be trimmed away based on the identification of a crossing, and which portions of the ray are kept. The algorithm sorts the points along the intersection ray based on the percent along the ray which they fall, and then locates where the calculated projected normal directions switch in sign. This switch is the indicator of an intersection with another limb patch, and therefore serves to show where the ray must be trimmed. In Fig. the point identified is 20% along the intersection ray, with a positive normal direction. The point which will delineate the trimmed portion of the ray is at 50% along the original ray, where the surface normal vectors have switched. The derivation of a surface normal direction is crucial for the process of delineating which points intersect on the body and which points intersect off the body and therefore should be discarded. The points that theoretically constrain the surface are what's left after a ray has been processed to find intersections meant to eliminate the points that extend



(a) Two adjacent edge planes with sampled points along the line of length L (b) Planes and their associated normal vectors: Two observations

Figure 2.7: Geometric Depiction of Patch Crossing Calculations

too far.

As the views are iterated over, the plane intersections are examined and a check is performed to find out if the plane segments are on the inside or outside of the silhouette using the calculation of the surface normal from Eq.3. The segments that are kept are not intersected at all, and therefore must represent our knowledge of where the surface is depending on the resolution of our observation data. As shown in Fig.one view overlaps with another view and two patches are found. One patch is formed from coplanar limbs and the green points represent the intersections saved. The other patch only intersects the first view on one side, so only one side of the original limb gets trimmed down and resampled. Both of the resulting patches, shown by the green planes, have new normal directions based on the normal directions of the limbs that were intersecting to form them.

After iterating through each view and trimming off the pieces of the rays that become intersected by another silhouette, the algorithm saves the remaining points as a point cloud output result. The segments of the original ray that are kept are the ones that were never intersected. This evaluation is strict and a misiden-

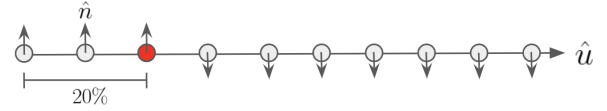


Figure 2.8: Intersection Ray from Two Patches -
Ten Sampled Points and Associated Ray
Normals

tified edge point could result in the trimming of necessary and correct surface data. This drawback is kept in mind during the tuning procedure of the Canny edge detection function, which is designed to be the least sensitive and therefore refined to only identify true edge points. Depending on the range of the observations about the target body, the surface can be resolved to different magnitudes. It is possible to localize using single-view geometry because of the assumption that range is known. Without this assumption, a multiple-view refinement of location using the coordination of edge points along epipoles within the image frame would be required. This estimation capability can easily be implemented in future iterations of this work in order to reduce assumptions and provide further autonomy to the method. However, in the scope of this work, it is assumed that the attitude and range are known quantities for our spacecraft. If a full equatorial survey is able

to be conducted, the resulting model will have more data and thus can be further refined by our method compared to a survey with less frequent observations taken. In the test cases presented in this paper, simulated data was used to represent an optimal scenario of observational ability. Using Blender blender, the case of a 0° phase angle could be simulated for maximum limb brightness and the elimination of a terminator. Data sets were collected for both Itokawa and Bennu, to examine the individual challenges of mapping an irregular shaped body versus a symmetric body.

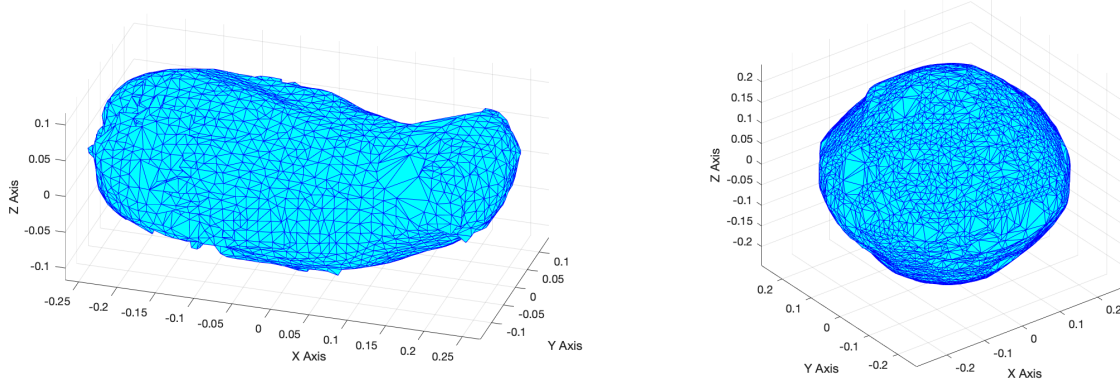
2.2.7 Outlier Rejection

Once the limb rays have been iterated on and their final intersections have been trimmed down, the remaining points and their associated surface normal directions are saved as 3D data suitable to represent a point cloud. In order to reconstruct a surface from the points, we first have to sample down the number of resultant points in order to eliminate outliers from a coarse trimming bias and promote a smoothing of the final surface Pomerleau2013. We also implement a function to filter out noisy particles Rusu2008. This function keeps any points that have 10 neighboring points within 1 standard deviation of the mean distance between all points in the point cloud.

2.2.8 Surface Reconstruction

Solving for the final surface involves implementing a method that calculates triangular facets and their associated normal unit direction. The method implemented in our work is a ball-pivoting approach that results in a completely closed manifold. The ball-pivoting method forms a closed shape from a point cloud using a ball with a pre-specified radius ρ . A triangular face is formed if the ball, initialized at a random point, contains no more than three points Bernardini1999. This ball moves along the edges of the triangles solved until it has reached every point available. From there, Delaunay triangulation is applied to find the optimal vertices for each facet and connect the shape as it would fit over a closed volume, as one would expect for a small body DiAngelo2011. These methods for reconstruction were chosen because of their geometric simplicity and their restriction to form a closed surface which is a requirement for any small body target. As shown in Fig.2.9,

we capture some of the finer details of the shapes despite the lower resolution of the limb-based method.



(a) Itokawa Surface Result

(b) Bennu Surface Result

Figure 2.9: Ball-Pivoting Surface Reconstruction Results of Itokawa and Bennu Point Clouds

2.3 Shape Results

2.3.1 Simulated Data

Using 21 simulated images of Itokawa and 11 images of Bennu, spaced 33° apart along both the equator and prime meridian of the bodies, generated in Blenderblender, we were able to resolve the following point clouds and the resultant closed mesh. We also report the shape model’s relative error compared to a high-resolution models of Itokawa and Bennu made using SPC Gaskell2006 from the Hayabusa and OSIRIS-REx missions, respectively. This error is calculated using a per vertex geometric distance between the measured mesh (built using iterative limb-trimming) and the reference mesh, or the detailed, high-resolution Gaskell models. We find that both models are extremely close to the truth, with error on the order of meters. Compared to more-precise methods that fit landmark data to maplets, our method gives similar results. The point-cloud post-processing steps are able to reduce the artifacts leftover from limb-trimming, typically observed as lines across the final surface. However, we would like to reduce the dependence on post-processing in future

works for the sake of retaining information about smaller features that our current algorithm was not refined enough to pick up, such as large boulders on Bennu.

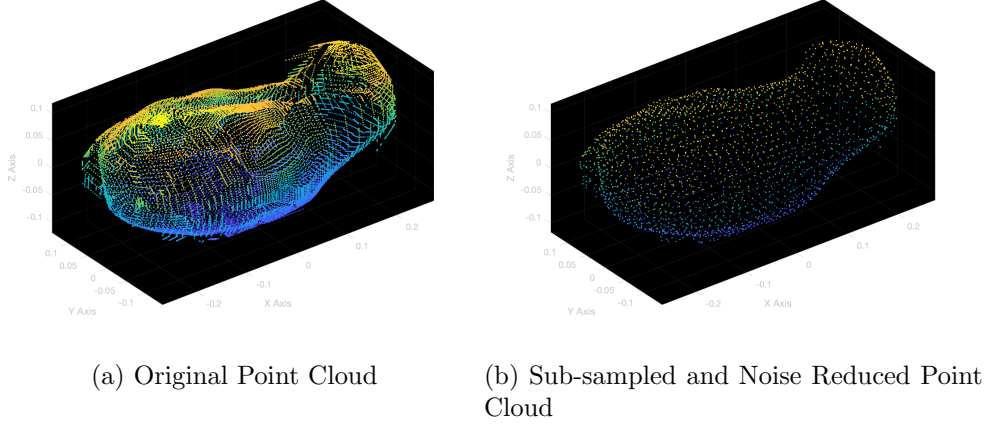


Figure 2.10: Pre- and Post-Processed Point Cloud of Itokawa Limb-Trimmed Shape

The reconstruction of Itokawa based on 21 simulated images is shown in Fig.2.11. The resultant shape is overall smooth along the surface, the concavities in the structure have been captured well based on the data survey, and the error in the shape when compared to a high-resolution model is between -22 and 33 meters, with an average surface error of -3 meters. The longest dimension of Itokawa is approximately 535 meters, which means that the body could be mismodeled up to 6 percent. The map shows that areas around the intersection with the x-axis present the most negative surface errors. This is believed to be caused by an assumption made about the rays extending from the camera frame to the edge of the body. The calculations described in previous sections assume that \hat{u} are straight, parallel when traced from the body to the camera. However, the images were captured at a relatively close distance where this assumption cannot hold without repercussions in the final shape. A better modeling technique would be to consider the line-of-sight vector from the center of the camera frame to the edge of the body, which extends as a cone shape.

The model shown here, developed using 11 images of Bennu along it's equator, is also a comparable shape result when measured against high-resolution models such as the 75cm surface

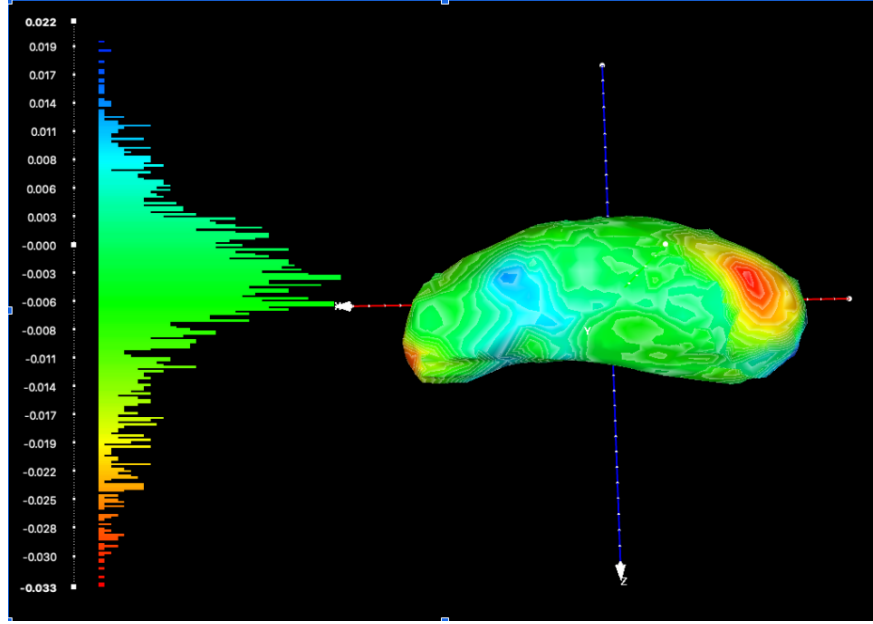


Figure 2.11: Limb-based Itokawa shape compared to SPC, with surface error in units of kilometers

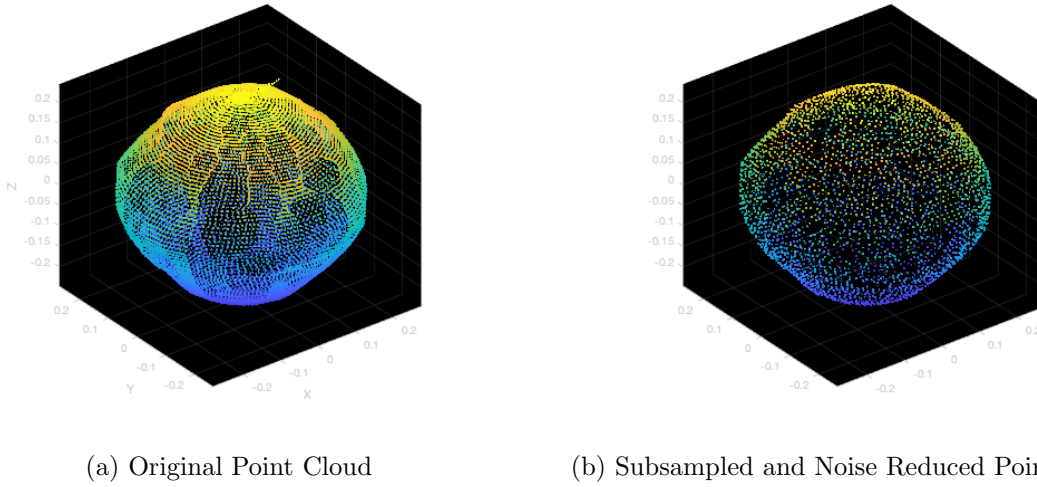


Figure 2.12: Pre- and Post-Processed Point Cloud of Bennu Limb-Trimmed Shape

model developed using observations made by OSIRIS-REx. The error found using the per-vertex geometric measuring approach is between -2.1 and 2.0 meters, with an average error of 0.5 centimeters. With the largest dimension of Bennu measuring at 565 meters, this represents a maximum mismodeling of 0.4 percent. This model has no predictable areas of under or over-estimation. The resulting shape is smooth, captures the size and general shape of the body, and could easily be

used in any proximity navigation solutions. Using data from a relatively close range, we expected the same perspective errors as were found in the Itokawa model, however, the simple convex shape of Bennu was easily and accurately mapped using its silhouette.

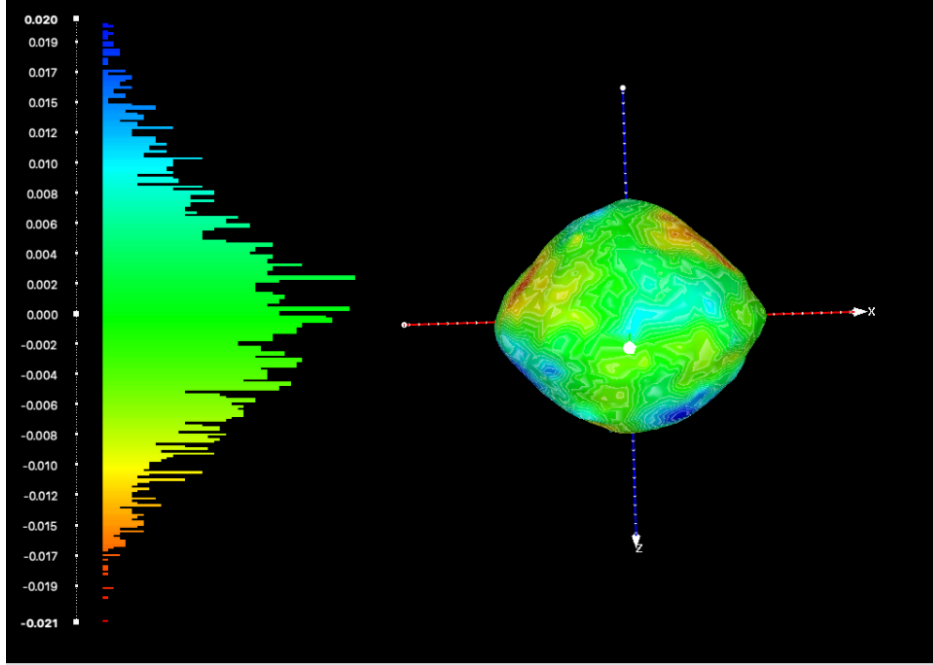


Figure 2.13: Limb-based Bennu shape compared to SPC, with surface error in units of kilometers

2.3.2 Mission Data

The last limb-trimmed shape model presented is developed using real mission images taken during the approach phase of the OSIRIS-REx mission by the PolyCam instrument. The major factor differentiating the previous simulated data models from the following model is the appropriateness of the zero degree phase angle assumption. For these reconstructions, we found views that had a low phase angle and therefore could easily ignore the terminator when searching for edge contours in the images without propagating large error in the model. It is to be expected that ignoring the phase angle between the sun and the body will always cause an under-determination of the shape by assigning the terminator as sunlit limb points. This drives forward future work in delineating terminator and limb from varying phase angles, however, the model presented here

works under the assumption that the body is always lit from behind the direction of the camera.

Implementing the same procedures as shown in previous sections, we were able to process 70 images of the asteroid Bennu using Canny edge detection for the silhouette identification and limb-trimming for shape resolution in order to build a surface model from these initial silhouette points. The results show that the model is biased towards underestimating the size of the surface, with the error spanning from -55 to 7 meters, and a mean error of -7 meters. As predicted, the phase angle assumption caused terminator points to be associated with the edge, therefore reducing the size estimate of the body as a whole based on the trimming scheme. However, the shape is reasonably captured based on the dimensions of Bennu and could be used for initial navigation when better data is not yet available.

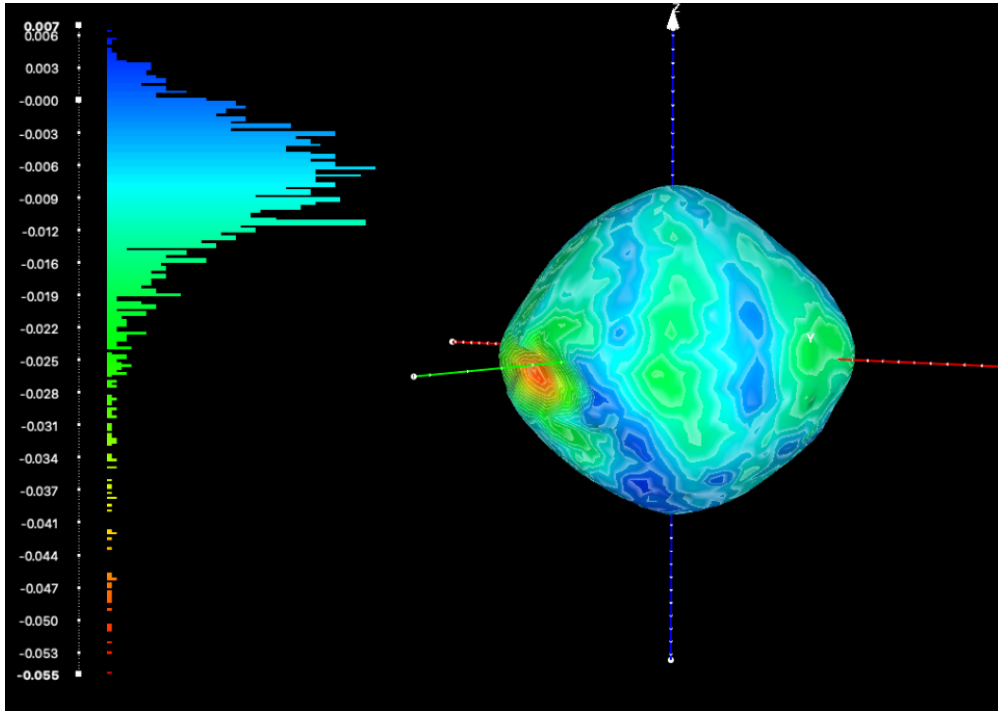


Figure 2.14: Bennu Shape Model from Real Images, compared to SPC, surface error in kilometers

2.4 Matching Localization

2.4.1 Method

The step of localization is important for any autonomous system to be able to navigate with the onboard generated map without human interference. Keeping a record of images with known locations about the body is one way to inform your future observations of their current orientation and range. We show a simplistic localization method based on finding correlations between test images and a library of images which were collected to build the initial model. With the asteroid Itokawa as our model, we use the Hayabusa mission image set from Oct. 1st, 2005 as the test images. The goal was to provide a test image with an associated latitude and longitude, and find the highest correlation score between this test image and the set of library images previously saved. Ideally, the highest correlation score would correspond to the same latitude and longitude between the test and library image. The process of correlation followed a simple iteration scheme where each test image was measured for a correlation score between each library image. We used a set of 36 library images of Itokawa generated in Blender with varying longitudes, spanning every 10 degrees. This library was acceptable for the images taken on approach, seeing as both the test images and the library set only greatly varied in the longitude orientation due to the spacecraft approaching the target body at an angle perpendicular to the spin axis on the day that the data was taken.

The correlation score is an important quantitative measure of similarity between images. This value, r , was measured between two binary images, and falls between 0 and 1, with 0 meaning no correlation between the images, and 1 meaning that the images have exactly the same pixel values for each location. The score used in this study was calculated as follows:

$$r = \frac{\sum_m \sum_n (A_{mn} - A)(B_{mn} - B)}{\sqrt{(\sum_m \sum_n (A_{mn} - A)^2)(\sum_m \sum_n (B_{mn} - B)^2)}} \quad (2.7)$$

In the correlation coefficient equation, m and n refer to the u and v axes of the images in question, A corresponds to the test image, B corresponds to the reference image, while \bar{A} and \bar{B} refer to the

two-dimensional mean of the pixel intensities in image A and B, respectively. The images in both the test set and the library were all 1024x1024 pixels. No stars were obvious in any of the test images, however, the test image corresponding to 89° was found to be flat.

2.4.2 Results

Correlating two images based on pixel values has proven to have some promise, however, our approach did not successfully match test images to the correct corresponding library image. The test case based on the asteroid Itokawa has shown that the body exhibits symmetries along certain axes that make it difficult for this correlation method to match the correct longitudes. We have learned that high correlation scores are possible between images that are meant to be matched, which shows that the 2-D correlation coefficient can see some similarities between images taken at the same longitudes. If this method were to be applied for localization procedures, it would need more rigorous matching capabilities. Shown in Fig.2.15, the two images presented are both focused on the same latitude and longitude, both 0° . The corresponding correlation coefficient is above 0.9, which means these images are a strong match to each other. However, the iteration scheme found another image in our library with a higher matching score and associated our test image with the incorrect image shown in Fig.2.16.

We can see from these comparisons that the algorithm failed to account for rotations in the body orientation. The expected match and the actual match have correlation scores within 0.005 of each other, showing that the algorithm can still correlate similarities well. However, this cannot be claimed as a success for navigation purposes seeing that the error in the matched longitude is 168.66° . Further analysis shows that for all of the images in the library, the score of the correlation between the library image and a test image follows a symmetric pattern, shown in Fig.2.17. If this method of localization was successful and we could match test images to their correct library equivalent, we would see the highest correlation scores following a $y = x$ trend across the score map. The observations made instead show that the highest correlation scores follow the symmetry of the body, and the most likely match in the images are when the asteroid is being viewed from the 0° and

Expected Match, NCC =0.92381

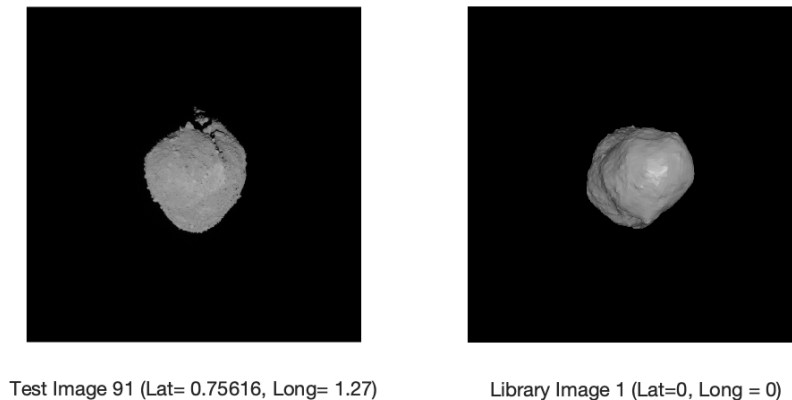


Figure 2.15: Test image and Library Image, Expected Match Pair

180° orientations. This data could be improved with further centering of test images during pre-processing, testing flipped orientations of the library images, or possibly examining the silhouette only for localization. Another avenue of testing could be for lighting-condition invariance, where many phase angles are tested and machine learning is applied to match features despite different sun anglesManni2020.

2.5 Analysis

2.5.1 Error Evaluation

The models generated with the limb-trimming method have been compared to mission-derived truth models of the same bodies. The 101955 Bennu shape model used for comparison is sourced from data during the approach phase of the OSIRIS-REx mission, and was made available publicly in November 2018. This model has a resolution of 6m over the surface. The 25143 Itokawa shape

Highest Scoring Matched Images, NCC =0.92712

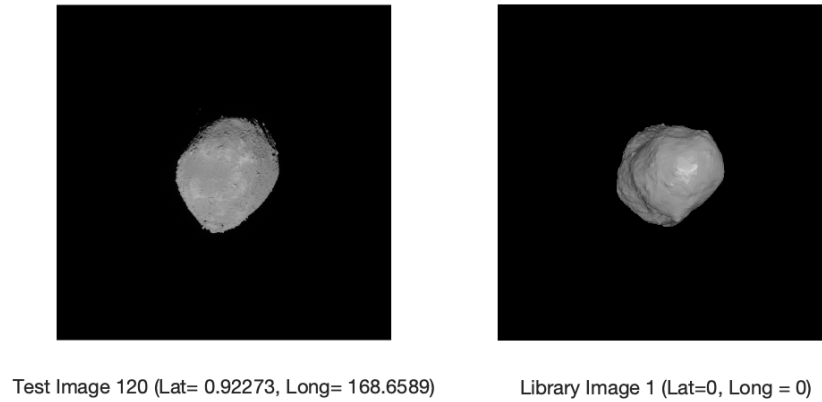


Figure 2.16: Test image and Library image, Actual Match Pair

model used for comparison is the Gaskell shape model produced with Hayabusa with a resolution of 49,152 facets Gaskell2004. A surface comparison between two shape models is performed using a Distance from Reference Mesh function, which calculates the closest distance from the reference mesh, or truth model, to the measured mesh, which is the model produced via limb trimming. The distance is left signed to appropriately characterize under- or over-estimated volumes.

2.6 Discussion

2.7 Conclusion and Further Work

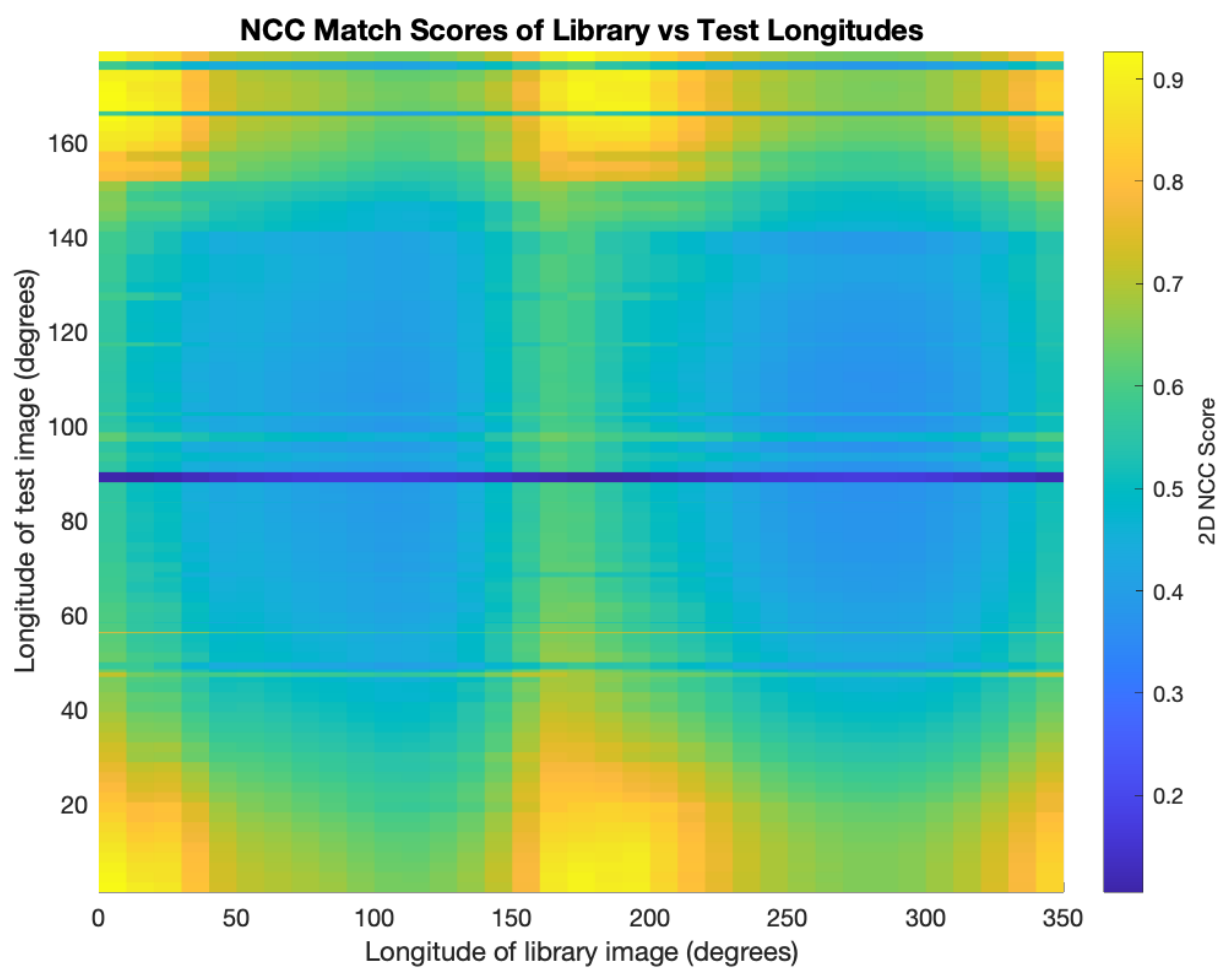


Figure 2.17: 2D Correlation scores between all library images and all test images, based on longitude

Chapter 3

Boulder-Induced YORP Altering Spin Acceleration

3.1 Torque Calculation

3.2 Boulder Factors

Chapter 4

Pole Stability and Obliquity Evolution under YORP Torques

Content

Chapter 5

Estimates of YORP for Ground-Based Observing

Content

Chapter 6

Future Work

Content

Bibliography

- [1] G. I. Baylor. Up, up and away. Proc. Roy. Soc., London A, 294:456–475, 1959.
- [2] M. E. Crow. Aerodynamic sound emission as a singular perturbation problem. Stud. Appl. Math., 29:21–44, 1968.
- [3] Julian D. Dole. Perturbation Methods in Applied Mathematics. Winsdell Publishing Company, 1967.
- [4] J. S. Fabnis, H. J. Gibley, and H. McDormand. Navier-stokes analysis of solid rocket motor internal flow. J. Prop. and Power, 2:157–164, 1980.
- [5] F. Guillot and Z. Javalon. Acoustic boundary layers in propellant rocket motors. J. Prop. and Power, 5:331–339, 1989.
- [6] IBM. SPSS Statistics. download from vendor site, 2012. version 21.
- [7] Henry Lao. Linear Acoustic Processes in Rocket Engines. PhD thesis, University of Colorado at Boulder, 1979.
- [8] Q. Lao, M. N. Cassoy, and K. Kirkpatrick. Acoustically generated vorticity from internal flow. J. Fluid Mechanics, 2:122–133, 1996.
- [9] Q. Lao, D. R. Kassoy, and K. Kirkkopru. Nonlinear acoustic processes in rocket engines. J. Fluid Mechanics, 3:245–261, 1997.
- [10] F. C. Mulick. Rotational axisymmetric mean flow and damping of acoustic waves in a solid propellant. AIAA J., 3:1062–1063, 1964.
- [11] F. C. Mulick. Stability of four-dimensional motions in a combustion chamber. Comb. Sci. Tech., 19:99–124, 1981.
- [12] R. S. Richards and A. M. Brown. Coupling between acoustic velocity oscillations and solid propellant combustion. J. Prop. and Power, 5:828–837, 1982.
- [13] T. M. Smitty, R. L. Coach, and F. B. Höndra. Unsteady flow in simulated solid rocket motors. In 16th Aerospace Sciences Meeting, number 0112 in 78. AIAA, 1978.
- [14] Joseph D. Taum. Investigation of flow turning phenomenon. In 20th Aerospace Sciences Meeting, number 0297 in 82. AIAA, 1982.
- [15] Robert A. Zeddini. Injection-induced flows in porous-walled ducts. AIAA Journal, 14:766–773, 1981.

Appendix A

Weird Exam Answers

About appendices: Each appendix follow the same page-numbering rules as a regular chapter; the first page of a (multi-page) appendix is not numbered. By the way, the following are supposedly authentic answers to English GCSE exams!

- (1) The Greeks were a highly sculptured people, and without them we wouldnt have history.
The Greeks also had myths. A myth is a female moth.
- (2) Actually, Homer was not written by Homer but by another man of that name.
- (3) Socrates was a famous Greek teacher who went around giving people advice. They killed him. Socrates died from an overdose of wedlock. After his death, his career suffered a dramatic decline.
- (4) Julius Caesar extinguished himself on the battlefields of Gaul. The Ides of March murdered him because they thought he was going to be made king. Dying, he gasped out: Tee hee, Brutus.
- (5) Nero was a cruel tyranny who would torture his subjects by playing the fiddle to them.
- (6) In midevil times most people were alliterate. The greatest writer of the futile ages was Chaucer, who wrote many poems and verses and also wrote literature.
- (7) Another story was William Tell, who shot an arrow through an apple while standing on his sons head.

- (8) Writing at the same time as Shakespeare was Miguel Cervantes. He wrote Donkey Hote. The next great author was John Milton. Milton wrote Paradise Lost. Then his wife died and he wrote Paradise Regained.
- (9) During the Renaissance America began. Christopher Columbus was a great navigator who discovered America while cursing about the Atlantic. His ships were called the Nina, the Pinta, and the Santa Fe.
- (10) Gravity was invented by Issac Walton. It is chiefly noticeable in the autumn when the apples are falling off the trees.
- (11) Johann Bach wrote a great many musical compositions and had a large number of children. In between he practiced on an old spinster which he kept up in his attic. Bach died from 1750 to the present. Bach was the most famous composer in the world and so was Handel. Handel was half German half Italian and half English. He was very large.
- (12) Soon the Constitution of the United States was adopted to secure domestic hostility. Under the constitution the people enjoyed the right to keep bare arms.
- (13) The sun never set on the British Empire because the British Empire is In the East and the sun sets in the West.
- (14) Louis Pasteur discovered a cure for rabbis. Charles Darwin was a naturalist who wrote the Organ of the Species. Madman Curie discovered radio. And Karl Marx became one of the Marx brothers.

Appendix B

Ode to Spot

(Data, Stardate 1403827) (A one-page chapter — page must be numbered!) Throughout the ages, from Keats to Giorchamo, poets have composed “odes” to individuals who have had a profound effect upon their lives. In keeping with that tradition I have written my next poem . . . in honor of my cat. I call it. . . Ode. . . to Spot. (Shot of Geordi and Worf in audience, looking mystified at each other.)

Felus cattus, is your taxonomic nomenclature
 an endothermic quadruped, carnivorous by nature?
 Your visual, olfactory, and auditory senses
 contribute to your hunting skills, and natural defenses.
 I find myself intrigued by your sub-vocal oscillations,
 a singular development of cat communications
 that obviates your basic hedonistic predilection
 for a rhythmic stroking of your fur to demonstrate affection.
 A tail is quite essential for your acrobatic talents;
 you would not be so agile if you lacked its counterbalance.
 And when not being utilized to aid in locomotion,
 It often serves to illustrate the state of your emotion.

(Commander Riker begins to applaud, until a glance from Counselor Troi brings him to a halt.)

Commander Riker, you have anticipated my denouement. However, the sentiment is appreciated.

I will continue.

O Spot, the complex levels of behavior you display
 connote a fairly well-developed cognitive array.
 And though you are not sentient, Spot, and do not comprehend
 I nonetheless consider you a true and valued friend.